Journal of Alloys and Compounds 507 (2010) L47–L53

Contents lists available at ScienceDirect

Journal of Alloys and Compounds

journal homepage: www.elsevier.com/locate/jallcom

Letter

Effect of phase transformation on structural, electrical and hydrophobic properties of nanocomposite $Ti_{1-x}Al_xN$ films

Vipin Chawla[a], Ramesh Chandra[a,*], R. Jayaganthan[b]

[a] Nano Science Laboratory, Institute Instrumentation Centre, Indian Institute of Technology Roorkee, Roorkee 247667, India
[b] Department of Metallurgical and Materials Engineering & Centre of Nanotechnology, Indian Institute of Technology Roorkee, Roorkee 247667, India

ARTICLE INFO

Article history:
Received 3 July 2010
Received in revised form 30 July 2010
Accepted 4 August 2010
Available online 11 August 2010

Keywords:
Sputtering
Nanocomposite films
Microstructural characterization
Contact angle
Resistivity

ABSTRACT

Nanocomposite $Ti_{1-x}Al_xN$ films were deposited on corning glass substrate by DC/RF magnetron sputtering in the present work. The effect of variation in Al content on structural features of $Ti_{1-x}Al_xN$ films has been investigated by characterization techniques such as XRD, FE-SEM, and AFM. The hydrophobic and electrical properties of the films have been measured by contact angle (Drop Shape Analysis System DSA100) (Kruss, Germany) and Four-probe method, respectively. XRD analysis of the $Ti_{1-x}Al_xN$ films with the variation in Al contents of $x_{Al} \leq 0.73$ and $x_{Al} \geq 0.78$ revealed the NaCl or cubic B1 structure and AlN wurtzite or hexagonal B4 structure, respectively. The crystallite size and lattice parameter of the films calculated from its XRD peaks revealed that it decreases with increasing Al contents. Structural analysis of the films has shown that with increasing Al contents (0.58 at.%), grain size decreases and pyramidal shape grains transforms into flowerlike structure and finally into disc like structure as evident from the FE-SEM analysis. The root mean square roughness of $Ti_{1-x}Al_xN$ films has decreased with increasing Al contents up to $x \leq 0.73$ (cubic B1 structure) but it increased when $x \geq 0.78$ (hexagonal B4 structure). The maximum contact angle of $123.8^\circ \pm 3.7^\circ$ (hydrophobic) has been observed for the $Ti_{1-x}Al_xN$ film with $x_{Al} = 0.17$ but it decreased continuously up to $x_{Al} = 0.73$ of Al content. However, contact angle of the films sharply increases again when the cubic B1 phase has transformed to hexagonal B4 structure at the $x_{Al} = 0.78$. The electric resistivity of $Ti_{1-x}Al_xN$ films has increased linearly in the cubic B1 structure but it increased sharply when the Al content exceeds $x = 0.73$ due to the phase transformation leading to formation of hexagonal B4 structure in the films.

1. Introduction

Titanium aluminum nitride ($Ti_{1-x}Al_xN$) coating was developed almost two decades ago, as a promising alternative to TiN coating, for providing better tribological and high temperature oxidation resistance to cutting and forming tools. It has been also used as diffusion barriers in microelectronics and electrodes in semiconductor devices [1–8]. An addition of Al to the TiN films by partial removal of Ti atoms increases oxidation resistance of the films at elevated temperatures due to the formation of a hard and protective layer of Al_2O_3 on the $Ti_{1-x}Al_xN$ surface. It has been reported that TiN with NaCl-type structure undergoes oxidation around 500 °C, but $Ti_{0.5}Al_{0.5}N$ is stable up to 700 °C [1]. It is well known that addition of Al contents to the TiN, preparation technique, and temperature affects the formation and structure of $Ti_{1-x}Al_xN$ films [1,9–13]. For example, the metastable solid solution of $Ti_{1-x}Al_xN$ with face centered cubic NaCl structure and hexagonal ZnS structure has been produced for the composition of Al varying between $0 < x_{Al} \leq 0.66$ and $x_{Al} > 0.66$, respectively with a substrate temperature of 350–550 °C in physical vapor deposition or plasma induced chemical vapor deposition techniques [1,14–16]. Upon annealing, the phase transformations has occurred in the metastable fcc-$Ti_{1-x}Al_xN$ solution ($x_{Al} \leq 0.66$) and it transformed into cubic Ti-rich and Al-rich domains, which exhibits higher hardness than the films with fcc structure [17].

Wahlstrom et al. [18] have investigated the sputter deposited $Ti_{1-x}Al_xN$ films and reported the following results such as (a) the $Ti_{1-x}Al_xN$ (0 0 2) films with variation of Al contents, $0 \leq x_{Al} \leq 0.52$ exhibits B1-NaCl structure; (b) two phase consisting of AlN-depleted $Ti_{1-x}Al_xN$ (0 0 2) grains and AlN-rich (0 0 0 2) and $(1 0 \bar{1} 1)$ grains showed B1-NaCl structure, and wurtzite-structure, respectively, for the Al contents varying between $0.52 \leq x_{Al} \leq 0.59$; for (c) single phase AlN-rich (0 0 0 2) and $(1 0 \bar{1} 1)$ grains with polycrystalline wurtzite-structure is observed for $0.59 \leq x_{Al} \leq 0.86$; and (d) single phase AlN (0 0 0 2) grains with wurtzite-structure is observed for $x_{Al} = 1$. It has been reported that the intensity of X-ray reflections from $Ti_{1-x}Al_xN$ films with $0.59 \leq x_{Al} \leq 0.86$ is very weak due to the formation of nanometer-sized grains and low-density interfaces,

---

* Corresponding author. Tel.: +91 1332 285869; fax: +91 1332 285243.
E-mail addresses: ramesfic@gmail.com, ramesfic@iitr.ernet.in (R. Chandra).

0925-8388/$ – see front matter © 2010 Elsevier B.V. All rights reserved.
doi:10.1016/j.jallcom.2010.08.017

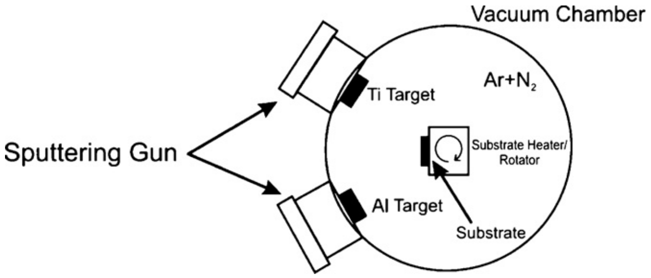

Fig. 1. Schematic diagram of experimental setup used for $Ti_{1-x}Al_xN$ films deposition.

confirming the formation of nanostructures in the films at these specific composition of Al. The phase transformation in $Ti_{1-x}Al_xN$ films with varying Al content, has been well studied in the literature [19–23]. However, structure and properties of the $Ti_{1-x}Al_xN$ films reported so far are widely different due to the different processing conditions chosen during deposition. The effect of phase transformation driven by changing Al contents in $Ti_{1-x}Al_xN$ films on electrical and hydrophobic properties of the films is scarce in the literature.

Hydrophobicity is an useful property when $Ti_{1-x}Al_xN$ is used as hard coatings on cutting tools and turbine blades as it precludes the harmful effect of wet surface. Recently, the coatings with multifunctional properties such as tribology, hydrophobicity, and electrical properties are being developed to improve the performance and life of the components exposed to various service conditions. Therefore, the present work has been envisaged to fabricate nanocomposite $Ti_{1-x}Al_xN$ films on corning glass substrate by using DC/RF magnetron sputtering and investigate the influence of phase transformation, induced by varying Al contents, on structural, electrical, and hydrophobic properties of films. The microstructural characteristics of $Ti_{1-x}Al_xN$ films were characterized by XRD, FE-SEM, and AFM. Contact angle measurement and Four-probe method were used to characterise the hydrophobicity and electrical properties of the thin films prepared under different processing conditions. The Al contents in the $Ti_{1-x}Al_xN$ films were analysed by using energy dispersive spectroscopy (EDS) attached with FE-SEM. The structural features and phase transformation of the films are correlated with their electrical and hydrophobic properties.

2. Experimental

2.1. Deposition of Ti–Al–N films

The $Ti_{1-x}Al_xN$ films were deposited on corning glass substrates by direct current (DC)/radio frequency (RF) magnetron sputtering system (Excel Instruments, India). DC magnetron sputtering is used for conducting targets such as metals or doped semiconductors but not for non-conducting targets (non-metals or insulators) because of its non-conducting nature, positive ions would lead to a charging of the surface and subsequently to a shielding of the electric field. Subsequently, the ion current would die off. Therefore, RF magnetron sputtering (radio frequency of 13.56 MHz) is used for non-conducting and semiconductor targets in which an AC-voltage is applied to the target. In one phase, ions are accelerated towards the target surface to sputter material and in the other phase, charge neutrality is achieved.

The sputtering targets were high purity (99.99%) Ti and Al metal disc (ACI Alloys, USA) of 2" diameter and 5 mm thickness, fixed at an angle of 45° to each other and with the use of rotator, the substrate was rotated between Ti and Al targets continuously to perform a co-sputtering as shown in Fig. 1. DC sputtering and RF sputtering for Ti and Al targets were used, respectively, during deposition of the films. Reactive cosputtering was used to deposit $Ti_{1-x}Al_xN$ films in the present work. The substrates were initially cleaned thoroughly in an ultrasonic bath of acetone and methanol and finally dried under nitrogen gas. Prior to sputtering deposition, the chamber was evacuated to a base pressure which was better than 2×10^{-6} Torr, achieved by turbo molecular pump backed by a rotary pump. Subsequently, the mixture of Ar and N_2 gases was introduced through a mass flow controller into the chamber. Before every sputtering run, the targets are pre-sputtered for 15 min with a shutter located in between the targets and the substrate in order to ascertain the same state of the targets in every run. This shutter is also used to control the deposition time. All the deposition was performed at a fixed substrate to target distance of approximately 5 cm. The sputtering parameters for $Ti_{1-x}Al_xN$ films with varying Al content are given in Table 1.

Table 1
Sputtering parameters for $Ti_{1-x}Al_xN$ films with variation of Al content.

Target	Titanium and Aluminum
Base pressure	2×10^{-6} Torr
Gas used	$Ar:N_2$ (85:15)
Sputtering pressure	10 mTorr
Deposition time	90 min
Sputtering power for Ti target	90 W
Sputtering power for Al target	0–180 W (0–0.81 at.%)
Substrate	Corning glass
Substrate temperature	550 °C

2.2. Characterization details

The orientation and crystallinity of the $Ti_{1-x}Al_xN$ films were studied using XRD (Bruker AXS, D8 Advance, Germany) with CuKα ($\lambda = 1.54$ Å) radiation in a $(\theta - 2\theta)$ geometry. The excitation voltage and current were set to a 40 kV and 30 mA respectively, in the diffractometer. The scan rate used was 0.2 sec/step with 0.02° increment and the scan range was from 25° to 55°. The crystallite size t of the $Ti_{1-x}Al_xN$ films was calculated by using the well known Scherrer's equation [24], given as

$$t = \frac{0.9\lambda}{B \cos \theta} \tag{1}$$

where, B (crystallite) is the corrected full-width at half maximum (FWHM) of a Bragg peak, λ is the wavelength of X-ray, and θ is the Bragg angle.

FE-SEM (FEI, Quanta 200F, Netherlands) was used to characterize the microstructures of the $Ti_{1-x}Al_xN$ films at an acceleration voltage of 20 kV and the atomic percentage of Al in the $Ti_{1-x}Al_xN$ films was measured by using energy dispersive spectroscopy (EDS) attached with FE-SEM at five different spots for each sample and the average value has been used. Cross-sectional FE-SEM images were used to measure the thickness of $Ti_{1-x}Al_xN$ films. The surface morphology of the $Ti_{1-x}Al_xN$ films was characterized by AFM (NT-MDT, Ntegra, Russia) operated in semi contact (tapping) mode. To calculate root-mean-square (RMS) roughness, five different spots for each sample was scanned using AFM and the average value has been used. The electric resistivity was measured by using Four-probe method at room temperature.

Contact angle of $Ti_{1-x}Al_xN$ films was measured by using Drop Shape Analysis System DSA100 (Kruss, Germany) in air at room temperature and the average contact angle value was calculated based on measurements at five different positions in each sample. The surface energy of $Ti_{1-x}Al_xN$ films has been calculated by Owens–Wendt method using two liquids with known surface energy values of 72.8 and 50.8 mN/m for water (polar component) and diiodomethane (dispersion liquid), respectively. When a liquid drop is in contact with an ideally smooth, homogeneous, rigid and insoluble solid, its equilibrium contact angle is expressed by Young's equation:

$$\gamma_L \cos \theta = \gamma_S - \gamma_{SL} \tag{2}$$

where, γ_L, γ_S and γ_{SL} are the surface energies of the liquid/vapor, solid/vapor and solid/liquid interfaces, respectively [25]. Fowkes [26] proposed that the surface energy (γ_S) can be described as the sum of contributions from dispersion interactions (γ_S^D) and non-dispersive interactions, which is also called the polar component (γ_S^P).

$$\gamma_S = \gamma_S^P + \gamma_S^D \tag{3}$$

Fowkes investigated mainly two-phase systems containing a substance (solid or liquid) in which the dispersion interactions are important across the interface and contribute to the work of adhesion, as expressed in the geometric mean of the dispersive surface energy. Hence, the surface free energy corresponding to the solid-liquid interface is calculated by the Eq. (4):

$$\gamma_{SL} = \gamma_S + \gamma_L - 2\sqrt{(\gamma_S^D \gamma_L^D)} \tag{4}$$

Owens and Wendt [27] extended Fowkes' equation and proposed a general form of expression:

$$\gamma_L(1 + \cos \theta) = 2\sqrt{(\gamma_S^D \gamma_L^D)} + 2\sqrt{(\gamma_S^P \gamma_L^P)} \tag{5}$$

where, the superscript D refers to the dispersion (non-polar) component, and P refers to the polar (non-dispersion) component, including all the interactions occurs between the solid and liquid, such as dipole–dipole, dipole-induced dipole and hydrogen bonding, etc. The solid surface energy is calculated using Eq. (5). Therefore, one could easily determine γ_S^D and γ_S^P by solving Eq. (5) using two liquids with known γ_L^D and γ_L^P for contact angle measurements.

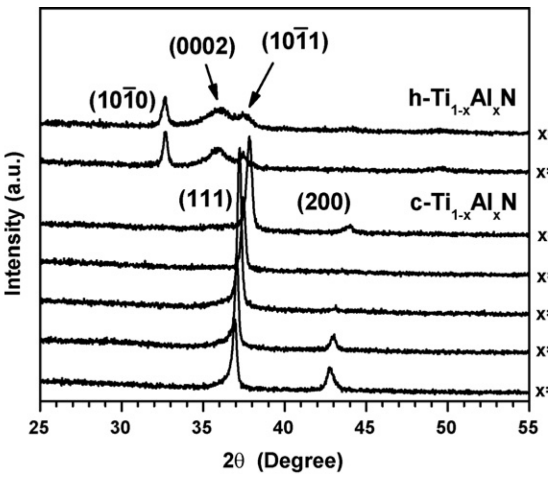

Fig. 2. XRD peaks of Ti$_{1-x}$Al$_x$N films with variation of Al content.

The influence of surface roughness on the water contact angle is expressed by Wenzel's equation [28]:

$$\cos\theta_W = A\cos\theta \tag{6}$$

where, A is a roughness factor, defined as the ratio of the real and apparent surface areas and θ_W is a water contact angle for a rough film surface. According to this relationship, the water contact angle for a rough but chemically homogeneous surface is larger than that of a smooth surface. On the other hand, when the film is smooth on the atomic scale, if the RMS roughness is below 0.5 nm, it does not affect surface energy. Hence, the effect of surface roughness on the water contact angle can be neglected and other factors are important as reported in the literature [29].

3. Results and discussion

Fig. 2 shows the X-ray diffraction patterns obtained from the nanocomposite Ti$_{1-x}$Al$_x$N films with x_{Al} = 0, 0.17, 0.35, 0.58, 0.73, 0.78, 0.81, respectively on corning glass substrate. It is observed that the XRD pattern at x_{Al} = 0 show the peaks of TiN (1 1 1) and (2 0 0) with NaCl or cubic B1 structure. With increasing Al content up to x_{Al} = 0.73, the peaks has gradually shifted to higher diffraction angle in proportion to the x_{Al} value, indicating a decrease in the lattice parameter value. The lattice parameter, a of Ti$_{1-x}$Al$_x$N films is calculated by using the equation of cubic structure given below [24]:

$$\frac{1}{d^2} = \frac{(h^2+k^2+l^2)}{a^2} \tag{7}$$

where, d is the interplanar distance obtained from the position of the (1 1 1) peak using the Bragg condition, a is the lattice parameter and h, k and l are planes. The change in lattice parameter was attributed to the substitution of Ti atoms with Al atoms (smaller atomic radius) in TiN with the cubic B1 structure as reported in the earlier literature [22,30,31]. Fig. 3 shows the effect of Al contents on the changes observed in inter planar spacing, d and lattice parameter, a of Ti$_{1-x}$Al$_x$N films with cubic B1 structure. The interplanar spacing and lattice parameters have decreased from 2.4324 Å and 4.213 Å for x_{Al} = 0, in pure TiN, to 2.3764 and 4.116 Å for x_{Al} = 0.73, in Ti$_{1-x}$Al$_x$N, respectively.

For films with $x_{\text{Al}} \geq 0.78$, new peaks appeared at positions close to those associated with the AlN wurtzite or hexagonal B4 structure. The cubic B1 structure for $x_{\text{Al}} \leq 0.73$ has transformed into hexagonal B4 structure for $x_{\text{Al}} \geq 0.78$, because of excess Al content. The positions of peaks were located at lower diffraction angles than those of AlN, therefore the lattice parameter became larger than that of AlN, presumably, because of the Ti$_{1-x}$Al$_x$N structure contains larger Ti atoms within the AlN exhibiting wurtzite or hexagonal B4 structure.

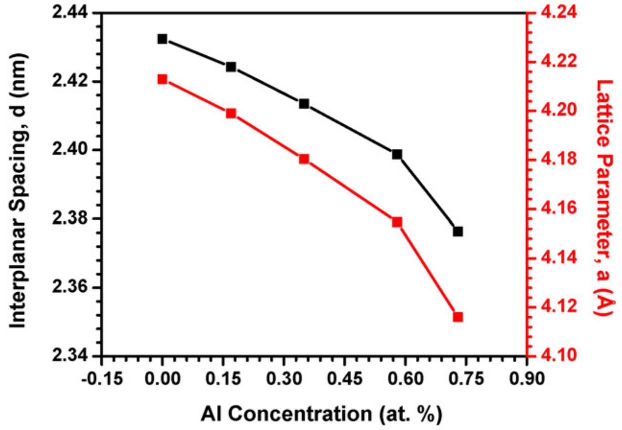

Fig. 3. Interplanar spacing and lattice parameters of Ti$_{1-x}$Al$_x$N films deposited with variation of Al content.

The crystallite size of the Ti$_{1-x}$Al$_x$N film with x_{Al} = 0 was calculated from the X-ray peak broadening is 41.4 nm and it decreases with increasing Al content. The size reduced to 13.9 nm for x_{Al} = 0.81. This is due to the inhibition of grain growth of TiN crystals due to the presence of second phase particles causing Zener drag effect. The inhibition of grain growth of a material due to the presence of second phase particle and impurities is called Zener drag effect. In the present work, when Al is doped in Ti$_{1-x}$Al$_x$N nanocomposite film, the Al particles inhibit the grain boundary mobility of TiN and suppress its grain growth due to Zener drag effect. For a random distribution of particles, the pinning force (p_z) exerted on the grain boundary is given by:

$$p_z = \frac{3\gamma F_v}{2r} \tag{8}$$

where, γ is the grain boundary energy, F_v is the particle volume fraction and r is the particle radius.

It indicates that TiN crystals become finer with the incorporation of the AlN phase. Fig. 4 shows the changes in crystallite size of all the Ti$_{1-x}$Al$_x$N films as a function of Al concentration.

The FE-SEM images of the Ti$_{1-x}$Al$_x$N films with increasing Al contents are shown in Fig. 5(a–e). From Fig. 5(a), uniformly distributed pyramidal shape grains are observed at x_{Al} = 0 and with increase in Al contents up to x = 0.58 (Fig. 5(b)), grain size decreases from 41.9 ± 2.9 to 29.0 ± 2.0 nm and there was no observable change in pyramidal grain morphology. However, when the Al content is increased above x_{Al} = 0.58 (Fig. 5(c)), pyramidal shape flowerlike

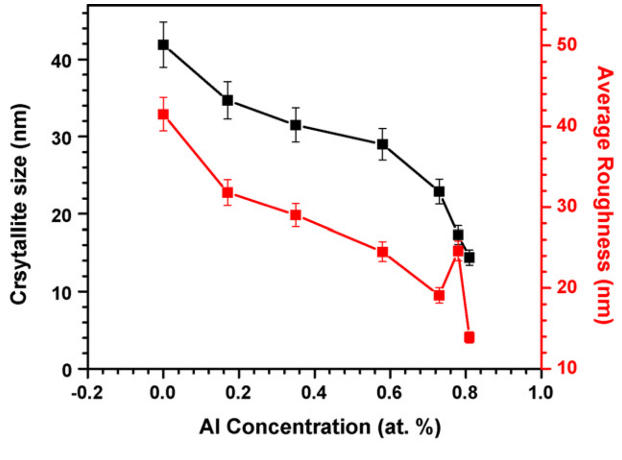

Fig. 4. Crystallite size and RMS roughness of Ti$_{1-x}$Al$_x$N films deposited with variation of Al content.

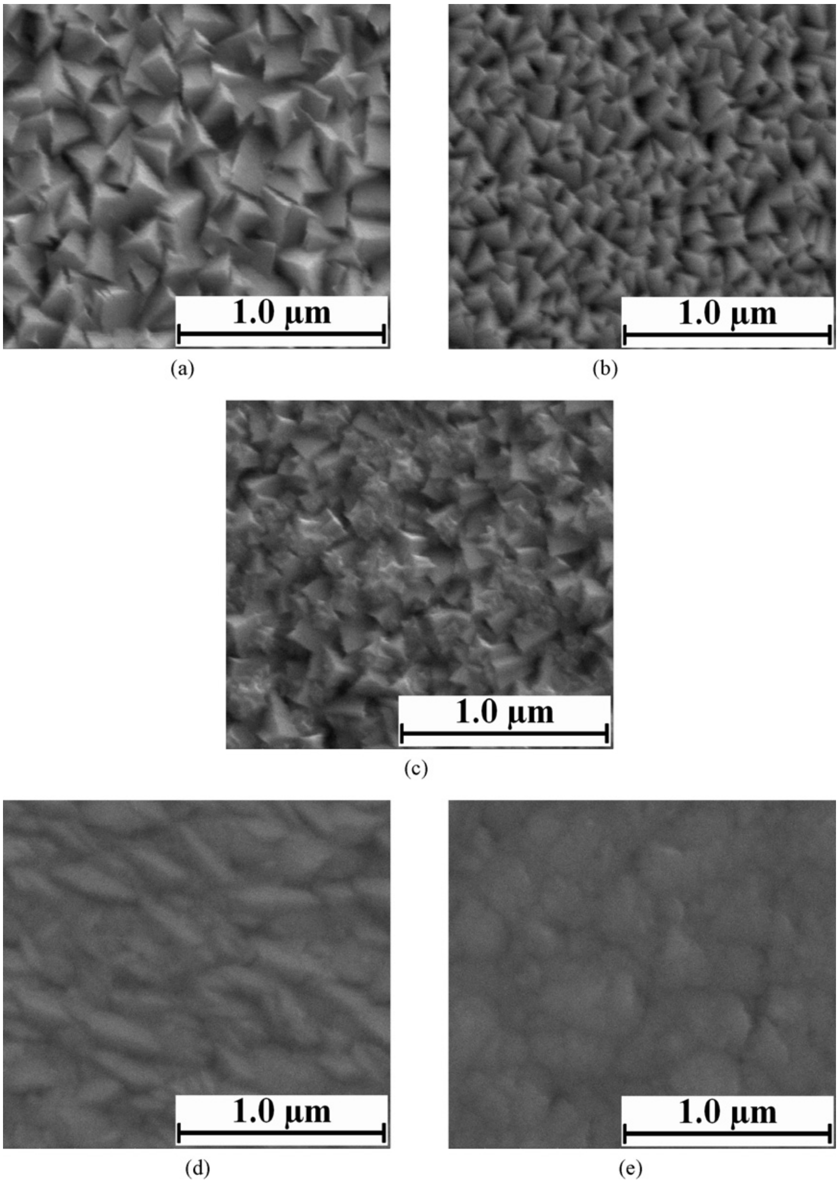

Fig. 5. FE-SEM images of $Ti_{1-x}Al_xN$ films with variation of Al content (a) $x = 0$, (b) $x = 0.35$, (c) $x = 0.73$, (d) $x = 0.78$ and (e) $x = 0.81$.

structure grains, and also tetragonal bipyramid grains are observed. With further increase in Al content up to $x_{Al} = 0.78$, cubic B1 structure has transformed into hexagonal B4 structure and the disc like structure has transformed into diffused structure when Al content, $(x_{Al}) = 0.81$. The reason of different grain shapes is that when the Al content is low ($x_{Al} \leq 0.58$), $Ti_{1-x}Al_xN$ shows the pyramidal structure, which is the structure of TiN. On further increasing the Al content, it becomes comparable to that of Ti and it shows pyramidal shape flowerlike structure and also tetragonal bipyramid structure. With further increase in Al content, it shows disc like structure which nearly matches to the structure of pure AlN. Hence, it can conclude that the structure depends on the concentration of Ti or Al and the higher concentration of these elements transforms the structure of $Ti_{1-x}Al_xN$ to its pure form. The atomic percentage of Al in the $Ti_{1-x}Al_xN$ films was calculated from the EDS results.

Fig. 6(a–e) shows the 2D AFM images of the $Ti_{1-x}Al_xN$ films with increasing Al contents and it is tandem with the FE-SEM results. It is evident from this figure that with increasing Al contents, surface roughness decreases, which could be explained from the XRD results in which X-ray peak broadening is observed indicating the size reduction of TiN up to Al content $x = 0.73$. With further increase in Al content, surface roughness increase initially due to the change in cubic B1 structure to wurtzite structure and finally decreases. The root mean square roughness values with different Al contents on corning glass substrate calculated from the AFM images of the films are plotted in Fig. 4.

Cross-sectional FE-SEM images of $Ti_{1-x}Al_xN$ film with varying Al content are shown in Fig. 7(a–b). It shows a columnar morphology and it becomes denser with increasing Al content. Since the atomic size of Al is smaller as compared to Ti atom, the doping of Al reduces the lattice parameter of the films as shown in Fig. 3, which leads to the formation of denser structure. The similar structure with increase in Al content of the films is observed as shown in cross-sectional FE-SEM micrographs of $Ti_{1-x}Al_xN$ films (Fig. 7). The film thickness is also increasing with increase in Al content because of the fixed power given to the Ti target; while increasing the power of Al target, which ensures the formation of thicker films. The thickness of $Ti_{1-x}Al_xN$ films measured from cross-sectional FE-SEM images are included in Table 2.

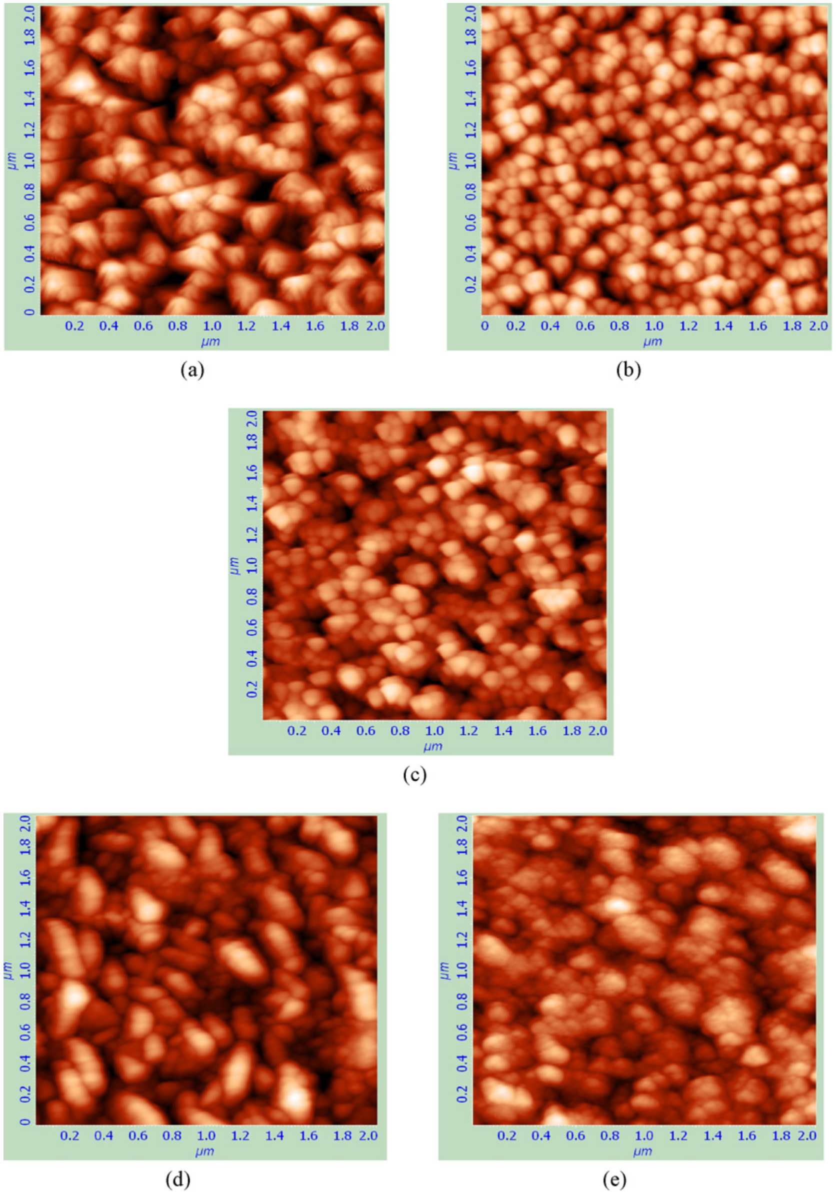

(a) (b) (c) (d) (e)

Fig. 6. AFM images of $Ti_{1-x}Al_xN$ films with variation of Al content (a) $x = 0$, (b) $x = 0.35$, (c) $x = 0.73$, (d) $x = 0.78$ and (e) $x = 0.81$.

Fig. 8(a–c) shows the contact angle between water and $Ti_{1-x}Al_xN$ films with varying Al content. Fig. 9shows the Al concentration (at.%) versus contact angle of all the $Ti_{1-x}Al_xN$ films. The corning glass substrate is hydrophilic in nature and showed average contact angle of 36.6° ± 1.1° for water. When tested for pure TiN film, the contact angle was 110.9° ± 3.3°. However, with Al content, $x_{Al} = 0.17$, in $Ti_{1-x}Al_xN$ film, the contact angle was 123.8° ± 3.7° (Fig. 8(a)). With further increase in Al content up to $x = 0.73$, the hydrophobicity has changed into hydrophilic and the contact angle was 18.1° ± 0.5°, which is less than the contact angle of bare substrate as shown in Fig. 8(b). In hydrophilic, the water droplet has spread quickly on the surface and permeated into the interior quickly, due to its high surface energy and vice versa for hydrophobic. However, the phase transformation from cubic B1 to wurtzite occurs when the Al content reached $x_{Al} = 0.78$ as evident from the XRD results shown in Fig. 2. Also, the contact angle increases sharply from 18.1° ± 0.5° to 122.5° ± 3.6° (Fig. 8(c)) for $x_{Al} = 0.73$ to $x_{Al} = 0.78$, respectively. The reason of contact angles variation with Al content is that the phases identified in pure TiN and AlN are cubic (B1 structure) and hexagonal (B4) structure, respectively. With increase in Al content, the contact angle decreases up to $x_{Al} = 0.73$ of Al content. The phase of the film at $x_{Al} = 0.73$ of Al content is still cubic B1 structure (shown in Fig. 2), which is TiN. However, with further increase in Al content ($x_{Al} = 0.78$), the structure of films transforms from cubic B1 structure to hexagonal B4 structure (shown in Fig. 2), and the contact angle increases up to 122.5° ± 3.6°. The contact angle of pure AlN films, deposited with same sputtering parameters, has been measured and it is found to be 121.4° ± 3.6°. The surface energy of $Ti_{1-x}Al_xN$ films which shows an inverse relation with contact angle is calculated by Owens-Wendt method by using Eq. (5) and included in Table 2.

TiN exhibits electrical conductivity similar to the metal, but AlN is a poor conductor. The electric resistivity of $Ti_{1-x}Al_xN$ film deposited on the corning glass substrates was measured at room temperature and plotted in Fig. 10. The electric resistivity of $Ti_{1-x}Al_xN$ films in the cubic B1 structure increases linearly. However, when the Al content (x_{Al}) is 0.78, the phase transformation from cubic B1 to wurtzite has occurred, increasing the resistivity of the films. Since, AlN is a very bad conductor, the electric resistivity of the $Ti_{1-x}Al_xN$ films has increased sharply

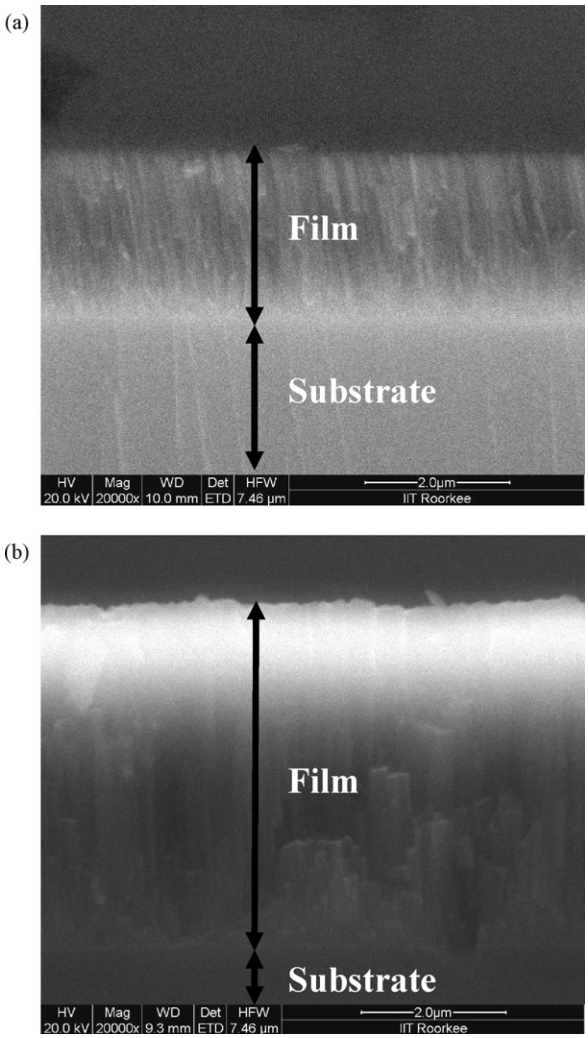

Fig. 7. Cross-section FE-SEM images of $Ti_{1-x}Al_xN$ films with variation of Al content (a) $x = 0.58$ and (b) $x = 0.81$.

Table 2
Properties of $Ti_{1-x}Al_xN$ films with variation of Al content.

S. no.	Sputtering power for Al (W)	$Ti_{1-x}Al_xN$ composition	Thickness (µm)	Surface energy, γ_S (mN/m)
(1)	0	$x = 0$	1.52	7.7
(2)	30	$x = 0.17$	1.30	3.7
(3)	60	$x = 0.35$	1.74	13.6
(4)	90	$x = 0.58$	2.29	62.5
(5)	120	$x = 0.73$	3.81	71.3
(6)	150	$x = 0.78$	4.17	4.0
(7)	180	$x = 0.81$	4.30	4.3

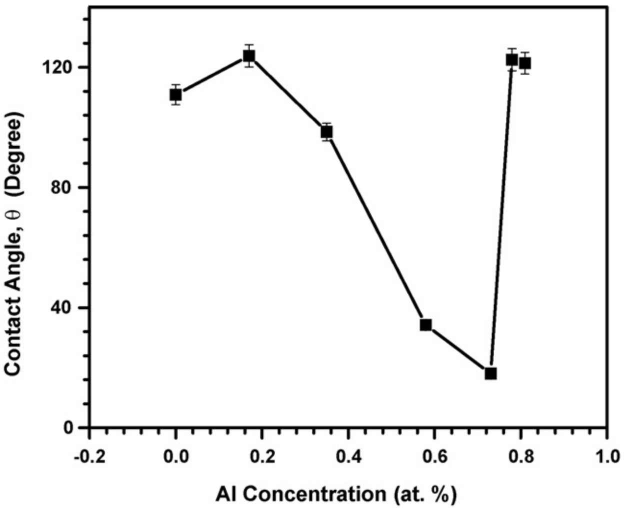

Fig. 9. Contact angle of $Ti_{1-x}Al_xN$ films deposited with variation of Al content.

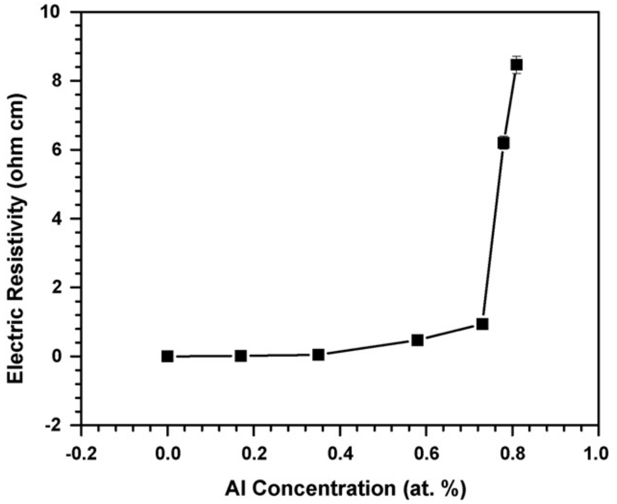

Fig. 10. Electric resistivity of $Ti_{1-x}Al_xN$ films deposited with variation of Al.

from 0.9 Ω cm for $(Ti_{0.27}Al_{0.73})N$ to 6.2 Ω cm for $(Ti_{0.22}Al_{0.78})N$. The reason is that the pure TiN is a semiconductor; while AlN is an insulator. With increase in Al content of $Ti_{1-x}Al_xN$ films, its resistivity increases slowly. This slow increase in resistivity continuous until $x_{Al} = 0.73$ of Al contents and phase of the films remain same as cubic B1 structure. With increase in Al content beyond $x_{Al} = 0.73$, structure of the films changes from cubic (B1) to pure AlN, i.e. hexagonal (B4) structure. Since AlN is a poor conductor, an abrupt increase in resistivity was observed. The observed electric resistivity values (0.9 Ω cm) for $Ti_{1-x}Al_xN$ with increasing Al concentration are in tandem with that of it reported

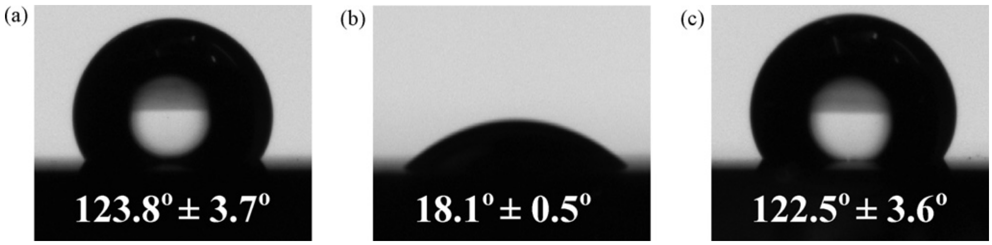

Fig. 8. Contact angle between water and $Ti_{1-x}Al_xN$ films with variation of Al content (a) $x = 0.17$, (b) $x = 0.73$ and (c) $x = 0.78$.

for the films deposited with varying nitrogen flow rate [31]. The similar trend in electric resistivity of $Ti_{1-x}Al_xN$ films has also been reported by Zhou et al. [23]. They have calculated resistivity of $Ti_{1-x}Al_xN$ films with varying Al concentration and observed a sharp increase of resistivity from 23.5 to 136 Ω cm, for $(Ti_{0.5}Al_{0.5})N$ and $(Ti_{0.4}Al_{0.6})N$, respectively. It may be mentioned that the increase in resistivity of $Ti_{1-x}Al_xN$ films as observed in the present work could be due to the formation of metal vacancies and reduction in grain size in the Al rich films [31] as well as due to the phase transformation occurs from cubic B1 structure to hexagonal B4 structure.

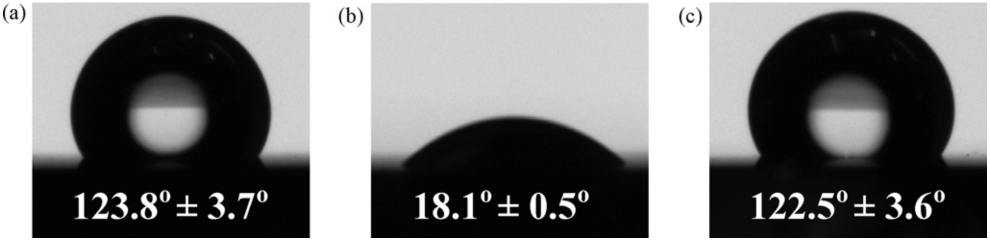

4. Conclusion

Nanocomposite $Ti_{1-x}Al_xN$ films were deposited on corning glass substrate by DC/RF magnetron sputtering. The influence of Al contents on structural properties of $Ti_{1-x}Al_xN$ films has been investigated by characterization techniques such as XRD, FE-SEM, and AFM. The contact angle and Four-probe method have been used to measure the hydrophobicity and electric resistivity of the films deposited with varying Al contents. XRD analysis of the $Ti_{1-x}Al_xN$ films, with varying Al contents, revealed the NaCl or cubic B1 structure up to $x_{Al} \leq 0.73$, beyond which at $x_{Al} \geq 0.78$, the film showed AlN wurtzite or hexagonal B4 structure. The crystallite size and lattice parameter decreases with increasing Al contents as observed from XRD results. With increasing Al contents, reduction in grain size occurs and pyramidal shape grains transforms into flower-like structure and finally into disc like structure. The root mean square roughness of $Ti_{1-x}Al_xN$ films, with increasing Al contents up to $x \leq 0.73$ (cubic B1 structure), decreases but it increases when $x > 0.73$ (hexagonal B4 structure). The maximum contact angle of $123.8^\circ \pm 3.7^\circ$ (hydrophobic) was observed for the $Ti_{1-x}Al_xN$ film of Al content $(x_{Al}) = 0.17$, which decreases continuously with increasing Al content. However, it increases sharply when the cubic B1 structure has transformed to hexagonal B4 structure when the Al content in the film exceeds 0.73. The electric resistivity of $Ti_{1-x}Al_xN$ films, in the cubic B1 structure, showed a linear trend but it increases sharply when x_{Al} exceeds the value 0.73 due to phase transformation.

Acknowledgement

The financial support by CSIR [Grant No. 03/0572NS/08/EMR II] New Delhi is gratefully acknowledged.

References

[1] W.-D. Münz, J. Vac. Sci. Technol. A 4 (1986) 2717–2725.
[2] O. Knotek, W.D. Münz, T. Leyendecker, J. Vac. Sci. Technol. A 5 (1987) 2173–2179.
[3] O. Knotek, M. Bohmer, T. Leyendecker, F. Jungblut, Mater. Sci. Eng. A 105 (1988) 481–488.
[4] W.D. Sproul, M.E. Graham, M.S. Wong, P.J. Rudnik, Surf. Coat. Technol. 61 (1993) 139–143.
[5] P.Eh. Hovsepian, Q. Luo, G. Robinson, M. Pittman, M. Howarth, D. Doerwald, R. Tietema, W.M. Sim, A. Deeming, T. Zeus, Surf. Coat. Technol. 201 (2006) 265–272.
[6] B. Alling, M. Odén, L. Hultman, I.A. Abrikosov, Appl. Phys. Lett. 95 (2009), 181906 (1–3).
[7] M. Beckers, C. Höglund, C. Baehtz, R.M.S. Martins, P.O.Å. Persson, L. Hultman, W. Möller, J. Appl. Phys. 106 (2009), 064915 (1–7).
[8] P.H. Mayrhofer, D. Music, J.M. Schneider, J. Appl. Phys. 100 (2006), 094906 (1–5).
[9] M. Wittmer, J. Noster, H. Melchior, J. Appl. Phys. 52 (1981) 6659–6664.
[10] O. Knotek, M. Bohmer, T. Leyendecker, J. Vac. Sci. Technol. A 4 (1986) 2695–2700.
[11] H.A. Jehn, S. Hofmann, V.-E. Ruckborn, W.-D. Münz, J. Vac. Sci. Technol. A 4 (1986) 2701–2705.
[12] W.-D. Münz, Werkst Korros 41 (1990) 753–754.
[13] T. Leyendecker, O. Lemmer, S. Esser, J. Ebberink, Surf. Coat. Technol. 48 (1991) 175–178.
[14] Y. Tanaka, T.M. Gur, M. Kelly, S.B. Hagstrom, T. Ikeda, K. Wakihira, H. Satoh, J. Vac. Sci. Technol. A 10 (1992) 1749–1756.
[15] T. Suzuki, Y. Makino, M. Samandi, S. Miyake, J. Mater. Sci. 35 (2000) 4193–4199.
[16] O. Knotek, T. Leyendecker, J. Solid State Chem. 70 (1987) 318–322.
[17] P.H. Mayrhofer, A. Hörling, L. Karlsson, J. Sjölen, T. Larsson, C. Mitterer, L. Hultman, Appl. Phys. Lett. 83 (2003) 2049–2051.
[18] U. Wahlstrom, L. Hultman, J.-E. Sundgren, F. Adibi, I. Petrov, J.E. Greene, Thin Solid Films 235 (1993) 62–70.
[19] L. Hultman, G. Hakansson, U. Wahlstram, J.-E. Sundgren, I. Petrov, F. Adibi, J.E. Greene, Thin Solid Films 205 (1991) 153–164.
[20] J. Musil, H. Hruby, Thin Solid Films 365 (2000) 104–109.
[21] H. Ohnuma, N. Nihira, A. Mitsuo, K. Toyoda, K. Kubota, T. Aizawa, Surf. Coat. Technol. 177/178 (2004) 623–626.
[22] A. Kimura, H. Hasegawa, K. Yamada, T. Suzuki, Surf. Coat. Technol. 120/121 (1999) 438–441.
[23] M. Zhou, Y. Makino, M. Noose, K. Nogi, Thin Solid Films 339 (1999) 203–208.
[24] B.D. Cullity, S.R. Stock, Elements of X-ray Diffraction, third ed., Prentice Hall, New York, 2001.
[25] T. Young, Philos. Trans. R. Soc. Lond. 95 (1805) 65–87.
[26] F.M. Fowkes, Ind. Eng. Chem. 56 (1964) 40–52.
[27] D.K. Owens, R.C. Wendt, J. Appl. Polym. Sci. 13 (1969) 1741–1747.
[28] R.N. Wenzel, J. Phys. Colloid Chem. 53 (1949) 1466–1467.
[29] J.-S. Chen, S.-P. Lau, Z. Sun, G.-Y. Chen, Y.-J. Li, B.-K. Tay, J.-W. Chai, Thin Solid Films 398/399 (2001) 110–115.
[30] W.D. Munz, J. Vac. Sci. Technol. A 4 (2004) 2717–2725.
[31] A.A. Irudayaraj, P. Kuppusami, S. Kalainathan, Surf. Eng. 24 (2008) 28–36.